Estimation of subcellular particle size histograms with electron microscopy for prediction of optical scattering in breast tissue

Matthew Bartek
Xin Wang
Department of Physics and Astronomy
Dartmouth College
Hanover, New Hampshire 03755

Wendy Wells
Department of Pathology
Dartmouth Medical School
Lebanon, New Hampshire 03756

Keith D. Paulsen
Brian W. Pogue
Thayer School of Engineering
Dartmouth College
Hanover, New Hampshire 03755

Abstract. Diffuse near-infrared tomography of tissue reveals scattering changes that originate from the submicroscopic features of the tissue; yet the existing tools to use this information to predict which features contribute to the scattering spectrum are limited by the lack of direct data quantifying the particle sizes. Breast tissue was examined with electron microscopy, and analysis showed that the distributions of particle sizes appear in double exponential functions for most cellular tissues. The average particle size histograms of high-grade cancer, low-grade cancer, fibroglandular tissue, and adipose tissue were examined. The particle histograms were progressively decreasing in magnitude for these tissue types, and the average size of the particles increased, for these four tissues, respectively. Typical particle sizes in the range of 10 to 500 nm for these tissue types, with biexponential fitting, gave two particle distributions: one near 20 to 25 nm for the smaller size and one at 110 to 230 nm for the larger distributions. Mie scatter theory was used to take these particle distributions and calculate scattering spectra. The ability to image reduced scattering coefficient spectra of bulk breast tissues exists, and so this data provides insight into how bulk imaging may be mapped over to predict factors related to the tissue ultrastructure. © *2006 Society of Photo-Optical Instrumentation Engineers.* [DOI: 10.1117/1.2398903]

Keywords: scattering; diffuse; particle; breast; cancer; electron microscopy.

Paper 06066RR received Apr. 9, 2006; revised manuscript received Aug. 16, 2006; accepted for publication Aug. 17, 2006; published online Dec. 28, 2006.

1 Introduction

The observed color of tissue comes from a complicated mixture of absorption by chromophores and scattering from features within the tissue.[1] While the composition of molecular absorbers in tissue are reasonably well predicted by individual spectra, the microscopic features that cause scattering spectra are considerably less easily predicted. This is mostly because of the complicated mixture of cellular, subcellular and extracellular features that cause scattering and because of the uncertainty of their contribution to the refractive index changes.[2–4] Nonetheless, many recent studies have shown that scattering parameters measured from tissue can be uniquely correlated to tissue substructure, function, and progression of disease.[5–9] Scattering could potentially used to measure response to therapy.[9] In ongoing tomography work, many groups are now examining the potential for diffuse tomography to characterize tissue, and scattering is thought to be a key feature indicating structural change, perhaps related to the density of subcellular features. It is generally thought that it may be possible to turn these measurements into estimates of effective particle size and density; however, there are significant assumptions and simplifications that must be made in this process, mostly related to the application of Mie scattering theory. In this study, one subset of these features is examined in detail, namely the distribution of particle sizes present in tissue. Both normal and diseased breast tissues are examined with electron microscopy (EM) to quantify the particle size histogram. These histograms are central to being able to estimate particle size and density from diffuse scattering tomography,[10–14] as well as to better understand how light interaction with tissue in general can be used to interpret microscopic features of the tissue.

Recent developments in extracting cellular and subcellular size and density features from tissues may have far-reaching applications, yet uncertainty about the "gold standard" of how to quantify particles that cause scattering in light is perhaps the most important part of this to be developed more fully. The central problem with having an independent way to measure particles that scatter light is that there is no clear way to measure them. The size scale is thought to be in the same range as the wavelength of light, but possibly extending well above and well below this size scale. Thus, the diffraction limitation of light imaging will not allow full resolution of these features, and any other measure will be a surrogate to this, as it will measure features with something other than

Address all correspondence to Brian Pogue, Thayer School of Engineering, Dartmouth College, 800 Cummings Hall, Hanover, NH 03755. Tel: 603 646-3867. Fax: 603 646-3856. E-mail: pogue@dartoutn.edu

Table 1 The tissue samples used in this study were analyzed with quantitative pathology estimates from immunohistochemical specimen slides to calculate the epithelial to stromal ratio (E:S), fat to stromal and epithelial rate (F:S/E), complete tissue type ratios, microvascular density (MDV), microvascular area (MVA).

Tissue (diagnosis)	E:S	F:S/E	Fibrosis/Fat/Epithelium	MVD	MVA
Normal breast	0.003	0.471	60/36/4	0.25	151
Normal breast	0.009	0.460	56/40/4	0.17	78
Normal breast	0.030	0.104	84/11/5	0.23	87
Infiltrating ductal carcinoma, low grade	0.166	0.040	6/3/91	1.02	75
Infiltrating ductal carcinoma, intermediate grade	0.214	0.011	0/0/100	0.85	74
Infiltrating ductal carcinoma, high grade	0.049	0.044	79/8/13	0.72	113

light. Van Staveren et al.[15] used EM to quantify the size distribution of Intralipid, a well-known and well-characterized scattering solution of emulsified lipids in water. They showed that the particle sizes were distributed as an exponentially decaying function with larger numbers of small particle sizes and significantly fewer of large sizes. They showed that estimates of this distribution provided an excellent way to estimate the bulk scattering coefficient spectrum of the solution. EM distinguishes electron dense versus nonelectron dense features of the tissue, and so membranes and areas of high-density protein and lipid content appear darker than areas of interstitial fluid or cytoplasm. To enhance the contrast, tissues are stained with uranyl and lead, so the uranyl binds to phosphates and lead acts as an enhancer to the signal. Phosphates are contained in large amounts in nucleic acids but are also present in membranes. There is considerable support for the belief that intracellular membranes are a major contributor to scattering, yet essentially all the data about this is correlative, and there is no independent measure of the size available. Thus, this part of the study remains a hypothesis, but will be examined in light of the resulting data.

A secondary goal of this study is to estimate the particle size distributions that result when using EM images, and then use these histograms to predict the reduced scattering coefficient that is observed in diffuse tomography. When measurements of diffuse tomography are taken, the transmission data is fit to diffusion theory, and there is no possibility of deriving the exact scattering coefficient spectrum, but rather the reduced scattering spectrum can be measured. The same spectrum can be estimated from Mie theory, and so the goal here is to examine the shape and magnitude of these spectra to see if they are similar. If similar spectra can be obtained, then it makes sense that diffusion theory–derived spectra could be used to estimate effective particle size and number density values and images. This has already been shown in previous studies; however, the justification for using the assumed exponential distribution of particle sizes was not validated prior to this present study.

The application of Mie theory to scattering measurements has a growing history, and yet the interpretation of whether it is appropriate is still unclear. Nonetheless, modeling the light scattering particles as spheres is one of the few tractable ways to proceed in using the scattering information, and care must be taken to interpret these parameters as "effective" Mie estimates. Much of the scattering in tissue is thought to be subcellular organelles such as mitochondria, lysosomes, Golgi bodies, vesicles, and so forth, all of which have sizes in the range of 50 to 500 μm or less.[16,17] Additionally, scattering from well-organized cells in culture have been studied extensively with a focus on estimating the scattering from the nuclei. Studies by Wax, Mourant, and Backman have all indicated that scattering from larger structures, such as the nuclei, could be present, but these are small signals superimposed upon the dominant scattering from smaller particles, which are significantly less than 1 μm in size.[6,18] While these are almost never spherical, individual photon events with the membranes would clearly interact with a radius of curvature, which might be considered spherical at the local level. In-depth modeling of Mie estimates of the scattering has consistently shown reasonable results under the assumption of the particles being spherical. However, it is also possible to consider that the scattering from subcellular organelles should be viewed as a coated sphere or shell shape, where the membrane is a thin layer over another medium. Wilson et al.[9] have shown that this gives a good estimate based upon angle resolved reflectance from cell suspensions undergoing apoptosis. Mie theory estimates of the scattering from shells have been well developed and are examined in the present study as possible ways to model the scattering, given the estimates of the particle distribution histogram. Both of these modeling approaches are examined using particle histogram data, with the goal of determining which assumed model fits the data more optimally.

2 Materials and Methods

2.1 Tissue Sample Processing and Immunohistochemistry

Immediately after excision, three cases of normal breast (reduction mammoplasty specimens) and three infiltrating ductal
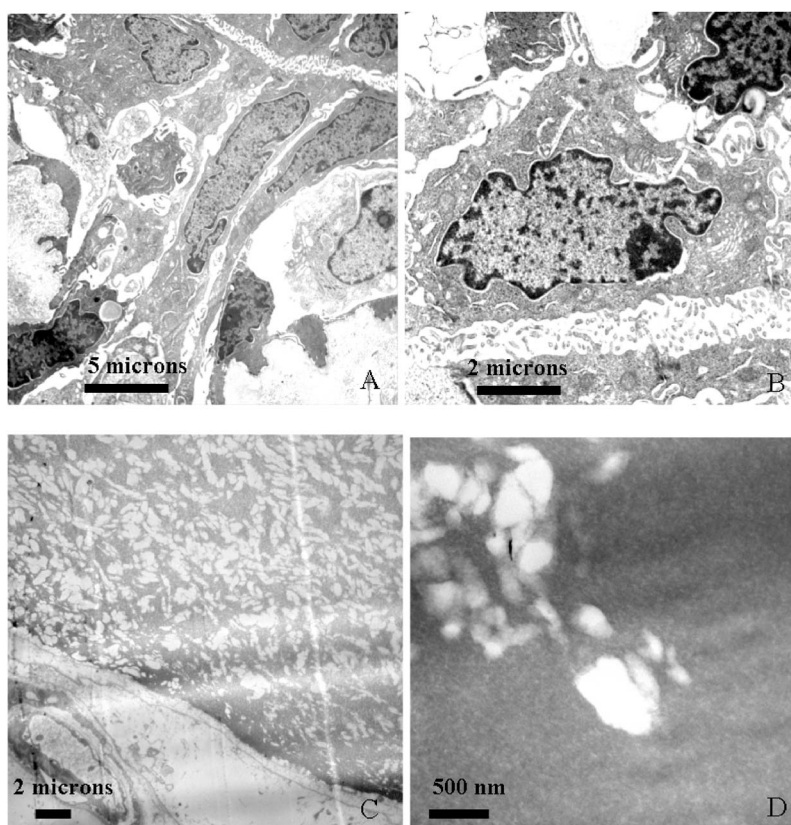
Fig. 1 EM images of normal fibroglandular tissues (a) and (b) at magnifications of 4000× and 9900×, respectively. Adipose tissue example images are shown in (c) and (d), at 4000× and 29 000×, respectively.

carcinomas of breast were evaluated in the Department of Pathology, sampled according to standard diagnostic protocols, and processed routinely (formalin fixation, alcohol dehydration, paraffin embedding). Each tissue specimen was taken from a different subject. A diagnosis was rendered on 4 μm-thick, routinely stained (hematoxylin and eosin) tissue sections. The histologic details are given in Table 1. Representative tissue sections from each case were also immuno-histochemically stained using the pan-cytokeratin marker 5D3 (which highlights the epithelial component in the tissue) and the pan-endothelial marker CD31 (which highlights the endothelial-lined vascular channels). Tissue type ratios [epithelium compared to fat and stromal fibrosis (E:S), fat compared to epithelium and stromal fibrosis (F:S/E), mean vessel density (MVD), and mean vessel area (MVA)] were assessed quantitatively using image processing techniques as described in a previous paper.[19] Using optimized color images from each slide, an automated macro in NIH IMAGE was used to count vessel density and area based upon the grayscale thresholded outline of the vessels. Unbiased estimates of volume density for each tissue type (fat, stromal fibrosis, and epithelium) in the tissue were obtained using point-counting stereology techniques.

2.2 Electron Microscopy

For each of the six cases, 2-mm³ portions of fresh breast tissue were fixed in 5 cc of 4% buffered glutaraldehyde for at least 2 h at 4 °C, then placed in 0.1 M of sodium cacodylate buffer at 4 °C for at least 15 min up to a week. From each of the three normal breast specimens, separate areas of fat, connective tissue, and glandular tissue were sampled. From each of the three breast tumor specimens, a representative tumor was sampled. The tissue was then placed in 2% osmium tetroxide with 0.1 M of sodium cacodylate buffer for 1 h at 4 °C, followed by graded ethanol (50, 70, 90, 100%), and then by L. R. White (50, 75, 100%) washes. The tissue was embedded in L. R. White in covered gelatin capsules and allow to stand overnight at room temperature in a hood before being placed in a 60 °C oven for 22 to 26 h. The 0.5-μm thick sections were cut and stained with 1% toluidine blue, and selected areas were sectioned at 120-nm thickness, placed on 3.0-mm copper grids, and then stained with uranyl acetate and lead citrate. These samples were examined with a FEI Tecnai F20 FEG electron microscope, and images were taken at magnifications of 3500×, 4000×, 19 000×, 29 000× for the different tissues as appropriate to capture the relevant features of each sample. Representative images of normal tissue and diseased breast tissues are shown in Figs. 1 and 2, respectively.

2.3 Image Processing

Using the EM images, the intra- and extracellular particles were quantified based upon the contrast in the EM images. Information about the magnification of the image, the thickness of the section, and the size in pixels of the digital EM picture contributed to converting raw counts into particle den-
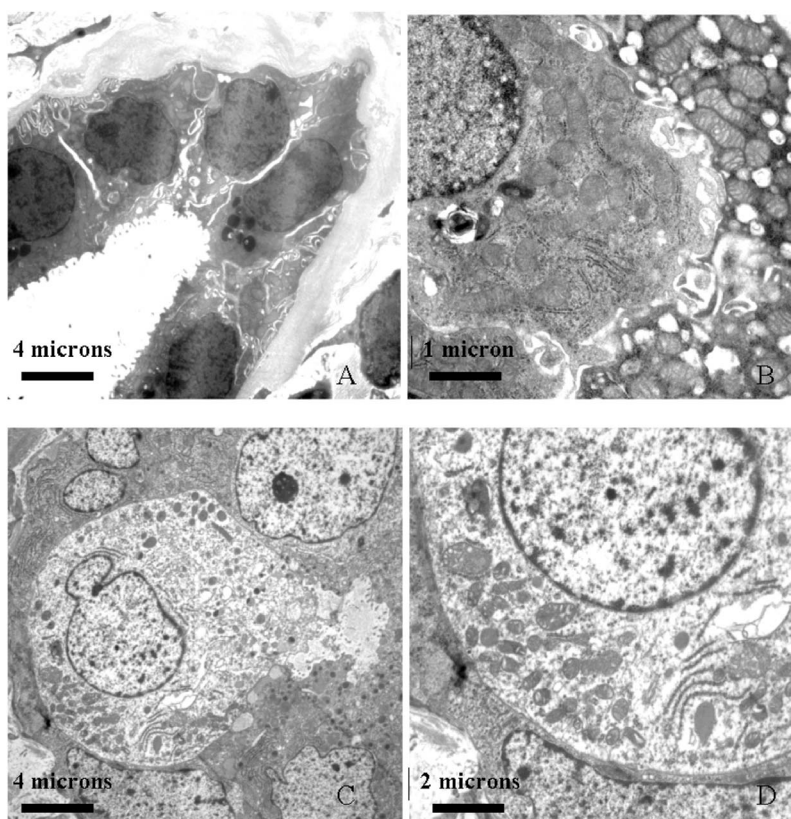
Fig. 2 EM images are shown of low-grade epithelial cancer (a) and (b) at 4000× and 9900× magnificiations. Similar images of a high-grade epithelial cancer are shown in (c) and (d) at 4000× and 15 000× magnifications.

sity values. The following calculation was done to achieve density dimensions of particles per cubic millimeters:

$$\frac{particles}{mm^3} = (\# \ particles)\left(\frac{\pi 66nm^2}{10 \ pixels}\right)\left(\frac{4000X}{Mag}\right)^2 (Area)$$
$$\times (Thickness)\left(\frac{1mm^3}{10^{18}nm^3}\right), \qquad (1)$$

where *Area* is the area in pixels of the image, *Thickness* is the thickness of the section set at 100 nm, and *Mag* was the magnification of the image, here used in the ranges of 4000× up to 29 000×, with a range of sizes for each tissue type. It was important to include multiple magnifications of images to increase the dynamic range over which the sizes could be reliably quantified. In the normal fibroglandular tissue, six separate images were analyzed; in the malignant epithelia, four images were quantified; and in the adipose tissue, three images were quantified, each on different ranges of magnification.

The same series of procedures were carried out on all images. The EM pictures were first thresholded in IMAGEJ, based upon a threshold. Varying thresholds were examined over the entire range of possible values, and all images were analyzed at five different threshold values. Early on in the study, it was determined that the threshold value varied the numbers of particles counted, but did not have a major effect upon the shape of the particle size histogram. Different methods were tried for choosing the threshold including simply stepping

through an equispaced set of threshold values, as well as setting the threshold on the maxima, minima, and points of inflection in the grayscale histogram distribution for each image. However, to avoid bias related to the choice of threshold, a equispaced range of threshold values were used for each image, and the resulting values were all pooled together for each image to create a composite of values for all thresholds. A single typical thresholded binary image is illustrated in Fig. 3(b), along with the original image Fig. 3(a).

In order to include large numbers of images, a morphological operator ANALYZE PARTICLES in the software package IMAGEJ was used to approximate the image as a conglomeration of ellipses and then measure the radii of each, thus establishing a particle size distribution. This feature of ImageJ works on binary images only, after thresholding, and counts particles that are dark and can be completely separated from other particles. Thus overlapping regions will be lumped together in this type of analysis, yet by varying the threshold value, it is possible to limit the effect of overlapping regions. The minimum and maximum allowable particle size was specified in units of pixels to be between 10 and 2500 pixels in size with 250 possible distinct sizes. Thus using images of differing magnification was important to expand the usable dynamic range. Figure 3(c) shows the resulting ellipse drawing after analysis of identifying particles. Figure 3(d) shows the output of this process: the histogram of the particle sizes composing the original image at a specific value for the threshold. As the particle size increased, the histogram of data points displayed
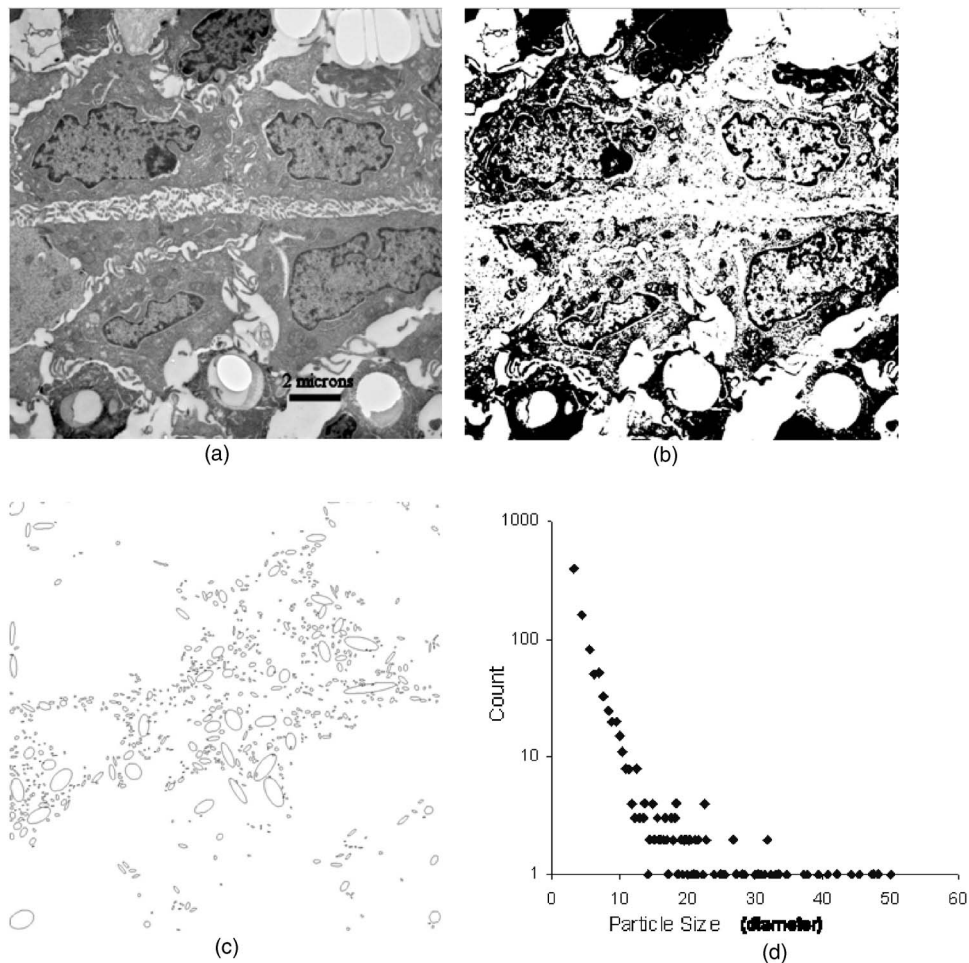
Fig. 3 (a) An original EM picture displaying approximately four epithelial cells with associated intra- and extracellular organelles and structure. After thresholding, (b) shows the binary representation of the original image for one particular value threshold value. In (c) the particle size analysis of the threshold image is shown where particles were represented by an ellipse of the approximate size. The results of this analysis are presented as a histogram of particle sizes in (d).

higher and higher variance, typical of poor statistics. The data points toward the end of the particle size range were disregarded when the variance reached 50% of the mean value, as these basically had very poor statistical power. The size range was expanded through the use of multiple magnifications of the EM images. The resulting histograms appeared to have a biexponential decay of particle size except for adipose tissue, which appeared to have a single exponential decay form to the histogram.

2.4 Mie Theory Numerical Implementation

Two MATLAB computer programs were used in this study, for simulating the sphere and shell data separately. The sphere code was adapted from a version produced by Dave Barnett, Loughborough University (http://www.lboro.ac.uk/departments/el/research/ photonics/matmie/mfiles.html) and the sphere and shell Mie code was adapted from the programs developed by Christian Matzler, Institute for Applied Physics, University of Bern (http://www.t-matrix.de/). The latter programs were used for simulation throughout this research and enabled a direct comparison between shell and spherical treatment. The functions used in this analysis were the calculation

of the Mie scatter efficiency (MIE.m) for estimating Q_{ext}, Q_{sca}, Q_{abs}, $Q_{backscat}$, $\langle \cos \theta \rangle$, Q_{ratio}. Based upon the inputs m and x, where m is the complex refractive index ratio and $x=k_o a$, with $k_o=2\pi/\lambda$ being the wave number in the medium and a being the particle radius. The program calculated the scatter coefficients a_n and b_n for given particle characteristics. The calculation of scattering from coated spheres is done with a MIECOATED.m program, which calculated the same Mie efficiencies with specified characteristics of the core and coating of the sphere. Inputs were the relative refractive indices of the core to the exterior medium and the coating to the exterior medium, respectively, along with the two radii of the spheres multiplied by the wave number of the medium. Estimates of the average cosine of the scattering angle and the scattering coefficient were done by calculating the parameters at all particle sizes within the histogram and weighting the distribution to the fraction of this distribution at this size. This was summed over all sizes for the final estimate of g, μ_s, and then also μ_s'.

The inputs of the optical constants of tissue came from Drezek et al.[8,20] and from Dunn's PhD thesis.[21] The index of the medium n_2 was set at 1.35 and the index of the sphere n_1
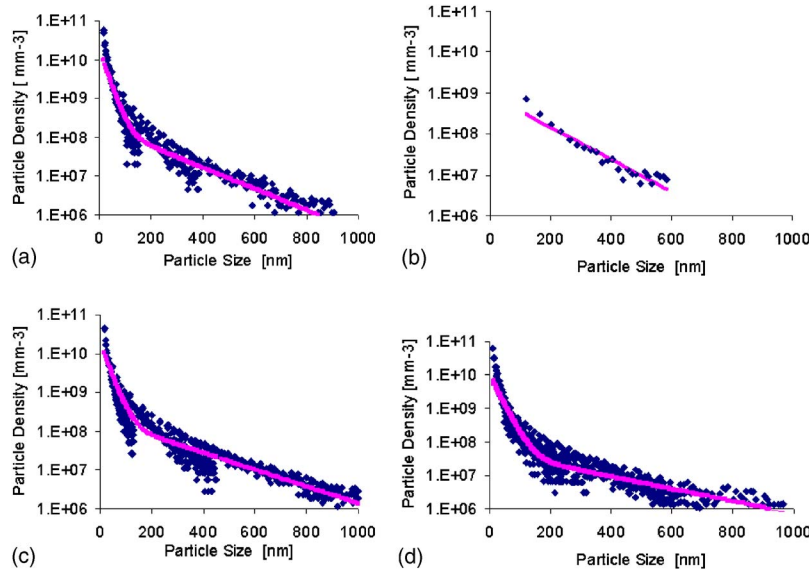
Fig. 4 Particle size distributions obtained by combining results from image processing as described in this paper: (a) normal fibroglandular tissue histogram; (b) normal adipose histogram; (c) high-grade epithelial tissue; (d) low-grade epithelial tissue.

at 1.40. These values correspond with experimental evidence of the indices of the cytoplasm and of the extracellular material. This yielded a relative index m of 1.04. For the shell treatment, the index of the medium was set at 1.35, the index of the shell n_2 at 1.46, and the index of the core n_3 at 1.35. This yielded relative indices, m_1 and m_2, of 1 and 1.0815, respectively. The thickness of the shell was taken to be 9 nm, corresponding to the estimated thickness and index of the bilipid membrane in cells and organelles.[21]

2.5 Comparing Mie Theory to Diffusion Theory

A central assumption in this work is that the scattering that is predicted by estimates of the particle sizes could then be directly compared to the estimate of scattering observed in bulk tissues, as quantified by fitting the signals to diffusion theory. As described above, the scattering coefficient for a distribution of particles is estimated by summing the scattering efficiency factor C_{sca} over all the particle sizes, weighted by the particle density histogram,

$$\mu_s(\lambda) = \sum_{i=1}^{n} C_{sca}(r_i,\lambda)N(r_i), \tag{2}$$

where $N(r_i)$ is the relative particle density as a function of particle size. Another useful quantity is the average cosine of the scattering angle, $g(\lambda)$, where more intense scattering is given more weight. $g(\lambda)$ is also called the anisotropy coefficient

$$g(\lambda) = \frac{\sum_{i=1}^{n} g(r_i,\lambda)C_{sca}(r_i,\lambda)N(r_i)}{\sum_{i=1}^{n} C_{sca}(r_i,\lambda)N(r_i)}. \tag{3}$$

In measurements from a highly scattering medium, these microscopic parameters do not hold much meaning, and so for tomographic measurements, it is more productive to assume that the scattering is isotropic and that under this assumption there is an effectively reduced scattering coefficient that is the inverse of the effective scattering length,[12] and this is mathematically estimated by

$$\mu_s'(\lambda) = \mu_s(\lambda)[1 - g(\lambda)]. \tag{4}$$

This final quantity is estimated in tomographic or bulk tissue measurements of the breast. Therefore, the results of this study will report variations of $\mu_s'(\lambda)$ with wavelengths for the different tissue types examined.

3 Results

The typical structures that can be viewed in EM can be seen in the images shown in Figs. 1–3. The fibroglandular tissues are dominated by epithelial cells and structural matrix components of collagen. In Fig. 1(a), there are several epithelial cells that can be found by their darker nuclear regions, which are distended in these cells and scattered in their interior. Around these nuclear regions, there are many mitochondria and other subcellular constituents. Basically the majority of the cellular interior is composed of bilipid layer bound organelles, as can be seen more clearly in Fig. 1(b).

Adipose tissue is distinctly different, with well-circumscribed fatty regions distributed across the image in

Table 2 Fitting parameter results for a double exponential decay model for the particle size histogram data shown in Fig. 4.

| Tissue	N_1	$\langle x \rangle_1$	N_2	$\langle x \rangle_2$
Normal fibroglandular	2×10^{10}	22.6	2×10^8	159
Normal adipose	—	—	9×10^8	110
Low-grade epithelium	9×10^9	27.2	8×10^7	196
High-grade epithelium	1×10^{10}	25.0	1×10^8	233

Fig. 5 The reduced scattering coefficient spectrum $\mu_s'(\lambda)$ is shown as calculated by (a) the solid spherical Mie theory calculation and (b) for the shell simulation of Mie theory, using the particle distribution histograms in Fig. 4.

Fig. 1(c). Close-up views of some of these are shown in Fig. 1(d). Cutting adipose sections is known to be difficult, due to the fact that the tissue does not solidify well and tends to smear during the cutting process. Thus, obtaining clear adipose sections for EM microscopy is challenging.

In carcinoma tissues, as shown in Fig. 2, the epithelial cells are more infiltrating and generally have larger nuclei and higher numbers of mitochondria. The overall pattern is highly variable and thus it is difficult to come up with standardized descriptions. However, representative images were taken from the low-grade and high-grade tumor sections examined, and images are shown at lower power and higher power in Fig. 2. Images (a) and (b) are the low-grade tumor, and (c) and (d) are the higher grade tumor.

The particle size distributions of these four tissue types were determined using multiple slices of the tissue and multiple imaging fields for each. Figure 3 shows the calculation procedure from a single image, with one histogram shown. Typically there were many small counts such as 1 or 2 at higher particle sizes, where the accuracy of the method breaks down. These lower points were typically eliminated from the histogram prior to pooling data from different images, as the error in accurately counting large particle numbers on high magnification was unacceptable. Instead of using these error prone counts at larger particle sizes, multiple magnification levels were used, such that three different ranges of particle sizes could be counted and combined on each graph, as is seen in the data display on Figs. 4(a), 4(c), and 4(d). Between two and four images were analyzed for each type. The results of each of the four tissue types is displayed in Fig. 4, and the results of the fitting to these data are shown in Table 2, with biexpoential fitting to the fibroglandular and cancer tissues, and single exponential fitting to the adipose tissue data. The best fit biexponential to the raw data points is shown on these graphs in Fig. 4, except for Fig. 4(b), which fit best to a single exponential. The adipose tissue histogram had a smaller range of particle sizes, mainly due to the observation that most fat particles existed within a smaller range of sizes, and thus the histogram of particle sizes in adipose was not as wide as observed in more heterogeneous tissue types such as fibroglandular tissue.

The raw data from each histogram was averaged at each particle size and used in Mie theory calculations to estimate the reduced scattering spectra and the anisotropy parameter. The calculations were done for all four tissue types, using both sphere and shell computations. Treatment of the scattering particles as spheres and as shells yielded a similar relationship between $\mu_s'(\lambda)$ and wavelength λ. However, the
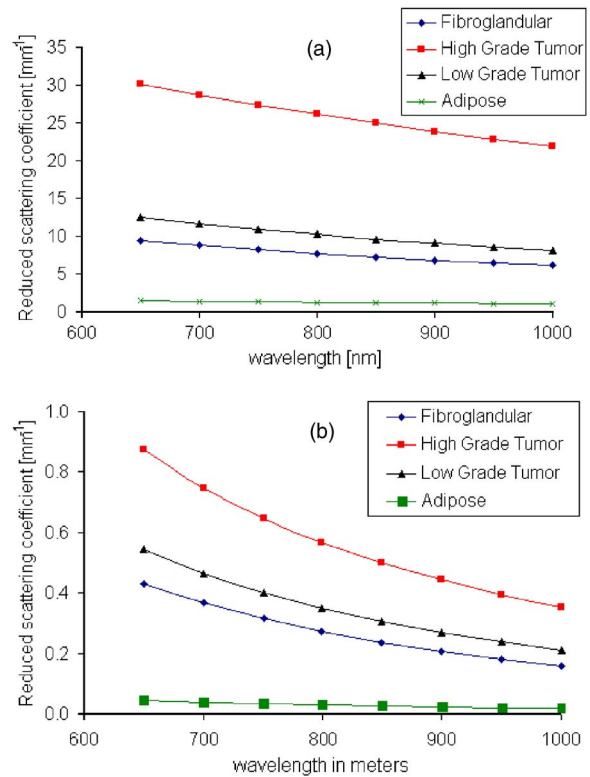
sphere plot in Fig. 5(a) is shifted vertically compared to the shell plot in Fig. 5(b). Charts depicting the spectrum of the anisotropy parameter are also included for completeness in Fig. 6.

Adipose tissue was consistently characterized by small $\mu_s'(\lambda)$ values and high-grade epithelial tissue with large ones. In fact, for both treatments, the order of high-grade, low-grade, fibroglandular, and adipose was preserved. In general, $\mu_s'(\lambda)$ values for the spherical treatment exceeded the expected values based on clinical data.[22–24] The shell treatment, however, generated values more in line with this clinical data. In both cases, $\mu_s'(\lambda)$ values for tumor tissue were clearly separate from those of normal tissue, showing some promise in the ability to use Mie theory–based calculations to catalog the scattering in breast tissue.

4   Discussion

In proceeding with the analysis of this study, it is important to recognize the underlying untested hypotheses that are implied in this and related studies that examine how light scatters in tissue. There are unfortunately quite a few untested questions, and this is largely due to the nanometer size scale being considered and the inability to find good tools to examine light scattering phenomenon at this size scale. Nonetheless, proceeding with the available tools may help migrate toward a common understanding of this. The current study is observational in nature and provides supporting evidence for the overall hypothesis that light scatters from membrane-bound sub-
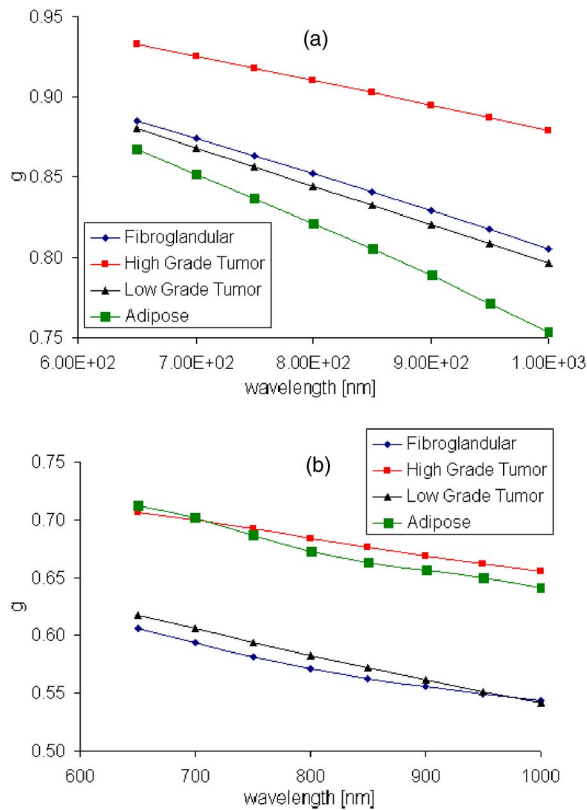
Fig. 6 The anisotropy coefficient spectrum $g(\lambda)$ is shown as calculated by (a) the solid sphere Mie theory and (b) the shell calculation, using the particle size histograms represented in Fig. 4.

cellular and extracellular structures that have a large range of sizes, weighted exponentially more toward the smallest observable scale.

A major assumption in the current paper is that cellular organelles and extracellular structures as observed in EM images accurately represent the same structures that cause light scattering in tissue. This is clearly a troubling assumption and yet the tools to objectively evaluate this are arguably lacking at the present time. The type of images shown in Figs. 1–3 show membrane-bound structures and areas of electron-dense subcellular features, due to the contrast mechanism in EM that preferentially provides contrast to these. This approach makes some sense, because there is data to support the idea that membrane-bound organelles contribute significantly to scattering,[25,26] and this is because of their change in refractive index from the background medium. Clearly it is possible that certain substructures observed in these images do not have the same change in index of refraction as others and contribute less to the overall scattered signal. If this is true, then this can potentially contaminate the results of the study. Hopefully future studies, possibly with near-field microscopy or phase contrast microscopy, could help to catalog maps of correlation between the observed structures in cells and that magnitude of scattering from each. Additionally, there can be concern that the tissue handling to prepare for EM might alter the tissue structure; however, the tissue is fixed prior to preparation, and so the only major deformation expected is in the preparation of fatty tissue, which is hard to cut in thin sections. However,

care was taken to try and obtain samples that were minimally distorted by the preparation and cutting prior to microscopy.

The choice of method to quantify the particle sizes in an automated way was another possible area of complication in the study, but one that was arrived at after rationalizing that hand counting of particles was simply inconceivable, due to the large sample sizes needed for each tissue type and the large number of particles present per image. Hand counting of selected slides was done and provided a consistent picture, although it has the complicating problems of observer bias in determining what is and is not a particle. After using grids overlaid on the images to attempt particle counting by hand, it was concluded that this was not clearly a reliable method for counting particles where the size range varied by over an order of magnitude, with potentially overlapping particles present. The only objective way to proceed was chosen as computer-assisted counting. Clearly this approach has problems, in that there is potential bias in the way that the image was thresholded and the way that the algorithm appeared to link regions that were perhaps independent particles yet appeared to be touching in the thresholded image. These are all valid criticisms, yet in the end when a large range of threshold values were used for any single image, the shape of the histogram resulting was always similar, with simply a change in the vertical offset. The type of data shown in Fig. 3 is very typical of the retrieved data in most images. The results indicate that the histograms of particle sizes are all effectively double exponential shapes, except for adipose tissue that appeared to have only a single exponential shape. These are consistent with an inspection of the images, which certainly shows a much larger number of small features as compared to the larger ones. This observation has very important implications for Mie theory or scatter theory modeling of the distributions, as they then present simple distributions, where the mean of the distribution (for a single exponential) is equal to the decay parameter. This feature makes modeling the distribution with a single parameter extremely useful. The overall number density (i.e., the numbers on the y axis in Fig. 4) are perhaps more questionable than the shape of the functions. While the quantitative estimates calculated in Eq. (1) are as accurate as can be achieved in this modeling, the question of threshold level clearly alters the observed number density. Thus, a major conclusion of this paper is that EM image analysis is reasonably good at estimating the average scatterer sizes, but potentially less accurate at estimating the absolute number densities of these particles.

There is another underlying hypothesis in this work: that Mie theory can be used to predict the scattering coefficient spectrum from the particle density histograms found with EM image analysis. This is directly examined, yet has several underlying untested hypotheses that could impact the interpretation of the results. Specifically, there is an assumption that the asymmetric patterns of membrane-bound organelles in tissue can be approximated as "effectively" spherical shapes or spherical shells, with respect to the more bulk scattered field values estimated in the Mie simulation. Again, this is a difficult point to address, and while literature exists to model scattering from cylinders as well, there is no clear path to modeling highly complex or even asymmetric shapes beyond the more complete approach of solving Maxwell's equations on assumed geometries. It is possible that EM-derived shapes

could be used as the input to Maxwell's equation solvers as was recently attempted by several researchers,[8,27,28] yet the computational power to do this in a systematic manner with a large number of particles is nontrivial. However, future studies could focus on this and perhaps shed light on this underlying assumption in breast tissue specimens.

Examining the predicted scattering spectra, the shell treatment produced values for $\mu_s'(\lambda)$ that were more in line with expectations based on experimental results; as in clinical studies, we observe that reduced scattering coefficient values are typically in the range of 0.5 to 1.5 mm^{-1}.[23] There is a large discrepancy in the μ_s values for the two treatments, where the shell treatment produces values in the range of $0 < \mu_s < 4$ and the sphere treatment produces values in the range of $0 < \mu_s < 450$. This difference is understandable because of the fact that there is simply less material to influence light when the scatterers are shells, despite an equal geometrical surface area. Therefore, at first glance, the shell treatment of scattering particles seems to catalogue the phenomenon best. The values of $\mu_s'(\lambda)$ give some reassurance to the validity of the assumption that the particle density is sufficiently low for Mie theory to apply legitimately. The units of $\mu_s'(\lambda)$ are inverse millimeters, and the shape of the curves match the general shape expected. The spectra of high-grade tumor tissue was significantly higher than that of low-grade tumor tissue, and fibroglandular tissue and adipose tissue were successively lower. These are almost exactly what is expected from previous *in vivo* imaging studies.[10–14]

The field of stereology prescribes a correction factor to account for the underestimation of the scattering particle radii due to the fact that if one cuts a sphere into thin slices, then averages the radii of the slices, the value of the average will be less than the actual radius of the sphere. Van Staverson et al.[15] omitted the correction factor noting that "larger particle sections are already over-represented. Thus the distribution is at least partly compensated (or even overcompensated) for the absence of a correction." However, because the sample thicknesses were 100 nm nominally, it should be expected that quantification of numbers of particles with size larger than this might be underrepresented, simply because they cannot be analyzed with full representation in these thinner slices. In fact this might lead to a slightly enhanced count rate in smaller particles due to the fact that larger particles that were sliced above or below their midpoint would appear smaller than their maximum diameter in most slices. Despite this potential artifact, it seems undeniable that the particle size histograms are heavily weighted to sizes smaller than 100 nm in all cases, except perhaps adipose tissue. The number of particles in the 10 to 50 nm range is clearly orders of magnitude higher than the number of particles above 100 nm, so while there is potential skew in the exact exponential fit, potentially biasing the distribution toward smaller particles, this bias is likely quite small due to the magnitude of the decay function. However, future studies with increasing thicknesses of samples done in EM could be used to analyze this issue, admittedly with significant effort to normalize the data for thickness change.

One last untested hypothesis in this work is that the particle density is sufficiently low to legitimately apply Mie theory. The development and application of Mie theory is based upon the single scattering event of a plane wave hitting a sphere or shell. Application of this model to bulk samples implies that the spacing between particles is sufficiently larger to allow each scattering particle to have a plane wave field interacting with it, and therefore, there are not inter particle field effects that would be sensitive to the density of packing. It is generally acknowledged that this approach is valid only if the mean particle spacing is at least 3 to 5 particle diameters, or stated alternatively, that the density of packing of particles is less than 10% of the volume. Clearly this latter statement is not true, as is shown in the images in Figs. 1 and 2, where it would appear to be at least 50% or more of the space is filled with scatters. However, once the particle counting is completed and the average scattering coefficients are estimated, the scattering coefficients are in the range of 1 to 50 mm^{-1}, leading to estimated mean free scattering lengths of 1 to 0.02 mm. If the "effective" scattering length is taken as the measure of particle density, then the average scattering events are spaced apart by 20 to 1000 μm, which is quite low compared to the sizes of the particles counted here (i.e., ranging from 1 to 1000 nm). Thus, the density factor appears to violate the 10% estimate of when Mie theory breaks down. Yet the range of sizes of particles effectively reduces the overall scattering coefficient to the point where interactions do not appear to be happening at the level that would cause violation of Mie theory prediction. However, this is clearly a unsatisfactory assessment and future work should examine this issue.

5 Conclusions

In summary, this report provides evidence for the fact that the particle sizes are distributed exponentially in subcellular structures, and that given assumptions about the index of refraction change, the shape of the scattering spectrum in the near infrared is consistent with what would be predicted by these particle size histograms. The estimation of scattering from Mie-theory shells has a better agreement with the observed magnitude of scattering in bulk breast tissue; however, this study is not conclusive in this area and further validation with well-controlled particle sizes would help determine which type of Mie theory should really be applied. It is likely that the most definitive part of this study is the predication of the average particle sizes for the different tissue types, which are all in the range of 110 to 230 nm, with the normal tissues being smaller in average size and the cancer tissues having larger average size. Adipose tissues seemed to have the most uniform size distribution, with only a single exponential distribution.

References

1. A. Kienle, L. Lilge, I. A. Vitkin, M. S. Patterson, B. C. Wilson, R. Hibst, and R. Steiner, "Why do veins appear blue? A new look at an old question," *Appl. Opt.* **35**, 1151–1160 (1996).
2. B. C. Wilson, M. S. Patterson, S. T. Flock, and J. D. Moulton, "The optical absorption and scattering properties of tissues in the visible and near-infrared wavelength range," *Light Biol. Med.* **1**, 45–52 (1988).
3. B. Beauvoit, H. Liu, K. Kang, P. D. Kaplan, M. Miwa, and B. Chance, "Characterization of absorption and scattering properties for various yeast strains by time-resolved spectroscopy," *Cell Biophys.* **23**, 91–109 (1993).
4. A. H. Hielscher, J. R. Mourant, and I. J. Bigio, "Influence of particle size and concentration on the diffuse backscattering of polarized light

from tissue phantoms and biological cell suspensions," *Appl. Opt.* **36**, 125–135 (1997).

5. L. T. Perelman, V. Backman, M. Wallace, G. Zonios, R. Manoharan, A. Nusrat, S. Shields, M. Seiler, C. Lima, T. Hamano, I. Itzkan, J. Van Dam, J. M. Crawford, and M. S. Feld, "Observation of periodic fine structure in reflectance from biological tissue: A new technique for measuring nuclear size distribution," *Phys. Rev. Lett.* **80**, 627–630 (1998).

6. J. R. Mourant, T. M. Johnson, and J. P. Freyer, "Characterizing mammalian cells and cell phantoms by polarized backscattering fiberoptic measurements," *Appl. Opt.* **40**, 5114–5123 (2001).

7. A. Wax, C. Yang, V. Backman, M. Kalashnikov, R. R. Dasari, and M. S. Feld, "Determination of particle size by using the angular distribution of backscattered light as measured with low-coherence interferometry," *J. Opt. Soc. Am. A* **19**, 737–744 (2002).

8. R. Drezek, M. Guillaud, T. Collier, I. Boiko, A. Malpica, C. Macaulay, M. Follen, and R. Richards-Kortum, "Light scattering from cervical cells throughout neoplastic progression: Influence of nuclear morphology, DNA content, and chromatin texture," *J. Biomed. Opt.* **8**, 7–16 (2003).

9. J. D. Wilson, C. E. Bigelow, D. J. Calkins, and T. H. Foster, "Light scattering from intact cells reports oxidative-stress-induced mitochondrial swelling," *Biophys. J.* **88**, 2929–2938 (2005).

10. B. Brooksby, S. Jiang, H. Dehghani, B. W. Pogue, K. D. Paulsen, J. B. Weaver, C. Kogel, and S. P. Poplack, "Combining near infrared tomography and magnetic resonance imaging to study in vivo breast tissue: Implementation of a Laplacian-type regularization to incorporate MR structure," *J. Biomed. Opt.* **10**, 050504-1–050504-10 (2005).

11. B. Brooksby, S. Srinivasan, S. Jiang, H. Dehghani, B. W. Pogue, K. D. Paulsen, J. Weaver, C. Kogel, and S. P. Poplack, "Spectral-prior information improves Near-Infrared diffuse tomography more than spatial-prior," *Opt. Lett.* **30**, 1968–1970 (2005).

12. S. P. Poplack, K. D. Paulsen, A. Hartov, P. M. Meaney, B. W. Pogue, T. D. Tosteson, S. K. Soho, and W. A. Wells, "Electromagnetic breast imaging—Pilot results in women with abnormal mammography," *Radiology* (in press) (2007).

13. X. Wang, B. W. Pogue, S. Jiang, X. Song, K. D. Paulsen, C. Kogel, S. P. Poplack, and W. A. Wells, "Approximation of Mie scattering parameters from near-infrared tomography of health breast tissue in vivo," *J. Biomed. Opt.* **10**, 051704-1–051704-10 (2005).

14. X. Wang, B. W. Pogue, S. Jiang, H. Dehghani, X. Song, S. Srinivasan, B. A. Brooksby, K. D. Paulsen, C. Kogel, A. P. Poplack, and W. A. Wells, "Image reconstruction of effective Mie scattering parameters of breast tissue in vivo with near-infrared tomography," *J. Biomed. Opt.* **11**(4), 041106 (2006).

15. H. J. van Staveren, C. J. M. Moes, J. van Marle, S. A. Prahl, and M. J. C. van Gemert, "Light scattering in Intralipid-10% in the wavelength range of 400–1100 nm," *Appl. Opt.* **30**, 4507–4514 (1991).

16. J. R. Mourant, T. Fuselier, J. Boyer, T. M. Johnson, and I. J. Bigio, "Predictions and measurements of scattering and absorption over broad wavelength ranges in tissue phantoms," *Appl. Opt.* **36**, 949 (1997).

17. V. Backman, V. Gopal, M. Kalashnikov, K. Badizadegan, R. Gurjar, A. Wax, I. Georgakoudi, M. Mueller, C. W. Boone, R. R. Dasari, and M. S. Feld, "Measuring cellular structure at submicrometer scale with light scattering spectroscopy," *IEEE J. Sel. Top. Quantum Electron.* **7**, 887–893 (2001).

18. A. Wax, C. Yang, V. Backman, K. Badizadegan, C. W. Boone, R. R. Dasari, and M. S. Feld, "Cellular organization and substructure measured using angle-resolved low-coherence interferometry," *Biophys. J.* **82**(4), 2256–2264 (2002).

19. W. A. Wells, C. P. Daghlian, T. D. Tosteson, M. R. Grove, S. P. Poplack, S. Knowlton-Soho, and K. D. Paulsen, "Analysis of the microvasculature and tissue type ratios in normal vs. benign and malignant breast tissue," *Anal Quant Cytol. Histol.* **26**, 166–174 (2004).

20. R. Drezek, A. Dunn, and R. Richards-Kortum, "Light scattering from cells: Finite-difference time-domain simulations and goniometric measurements," *Appl. Opt.* **38**(16), 3651–3661 (1999).

21. A. Dunn, "Light scattering properties of cells," PhD diss., University of Texas, Austin (1997).

22. S. Srinivasan, B. W. Pogue, S. Jiang, H. Dehghani, C. Kogel, S. Soho, J. G. Chambers, T. D. Tosteson, S. P. Poplack, and K. D. Paulsen, "Interpreting hemoglobin and water concentration, oxygen saturation, and scattering measured by near-infrared tomography of normal breast in vivo," *Proc. Natl. Acad. Sci. U.S.A.* **100**, 12349–12354 (2003).

23. B. W. Pogue, S. Jiang, H. Dehghani, C. Kogel, S. Soho, S. Srinivasan, X. Song, T. D. Tosteson, S. P. Poplack, and K. D. Paulsen, "Characterization of hemoglobin, water, and NIR scattering in breast tissue: Analysis of intersubject variability and menstrual cycle changes," *J. Biomed. Opt.* **9**, 541–552 (2004).

24. S. Srinivasan, B. W. Pogue, S. Jiang, H. Dehghani, C. Kogel, S. Soho, J. J. Gibson, T. D. Tosteson, S. P. Poplack, and K. D. Paulsen, "In vivo hemoglobin and water concentration, oxygen saturation, and scattering estimates from near-infrared breast tomography using spectral reconstruction," *Acad. Radiol.* **13**, 195–202 (2006).

25. B. Beauvoit, T. Kitai, and B. Chance, "Contribution of the mitochondrial compartment to the optical-properties of the rat-liver—a theoretical and practical approach," *Biophys. J.* **67**, 2501–2510 (1994).

26. B. Beauvoit, S. M. Evans, T. W. Jenkins, E. E. Miller, and B. Chance, "Correlation between the light-scattering and the mitochondrial content of normal-tissues and transplantable rodent tumors," *Anal. Biochem.* **226**, 167–174 (1995).

27. D. Arifler, M. Guillaud, A. Carraro, A. Malpica, M. Follen, and R. Richards-Kortum, "Light scattering from normal and dysplastic cervical cells at different epithelial depths: Finite-difference time-domain modeling with a perfectly matched layer boundary condition," *J. Biomed. Opt.* **8**, 484–494 (2003).

28. R. Williams, "Three-dimensional counting: Accurate and direct method to estimate numbers of cells in sectioned material," *J. Comp. Neurol.* **278**, 344–352 (1988).